ter δ was further reduced to obtain the HLLE scheme. Instead of introducing the HLLE switching function of Ref. 5, this was achieved by modifying Eq. (11). The pressure difference in σ_1 was replaced with

$$\sigma_1' = \Delta\rho - \Delta'p/\bar{c}^2 \tag{12a}$$

where

$$\Delta'p = \max(|\Delta p|, l_0 s/\mathrm{grad}\,p|) \cdot \mathrm{sign}(\Delta p) \tag{12b}$$

and

$$s = \begin{cases} 1, & \text{for} & u \cdot \mathrm{grad}\,p > 0 \\ 0, & \text{for} & u \cdot \mathrm{grad}\,p < 0 \end{cases} \tag{12c}$$

and where l_0 is the length scale and is typically unity. The switch s turns on the HLLE scheme only at strong compression regions. The pressure gradient was evaluated at the left and right cells with central differencing, and the larger of the two values was used in Eq. (12).

Results

The one-dimensional scheme, Eqs. (2), (5), and (11), solved the shock-tube problems tested in Ref. 3 satisfactorily. Thus the results are not shown here. The following results were obtained from the multidimensional version of the present scheme derived from the standard dimensional splitting technique.

Figure 1 shows computed pressure contours for the carbuncle problem. The freestream Mach number is 8 and an inviscid ideal gas is assumed. This computation was performed on a 101 × 61 grid. Figure 1a shows the pressure contours obtained with the present scheme (first-order accurate) using Eqs. (2), (5), (11), and (12). The result indicates a stable bow shock wave. Figure 1b shows the corresponding plot without using Eq. (12). The carbuncle phenomenon appears here.

Figure 2 shows the computed density contours of the conical flowfield over a 75-deg delta wing at a freestream Mach number of 2.8, angle of attack of 16 deg, and a Reynolds number of 3.565 × 10⁶. Laminar flow is assumed. The grid consists of 99 × 51 points. The present scheme was extended to third-order accuracy by using the MUSCL approach through the primitive variables.[6] The bow shock wave and the crossflow shock wave can be seen below and above the wing, respectively. The low density areas over the wing correspond to the primary and secondary vortices due to the flow separation at the leading edge. Figure 2a shows the result from the multidimensional version of the present scheme, while Fig. 2b shows the plots obtained from the HLLE scheme. The present result shows identical resolution to that of the Roe scheme. Without the switch, Eq. (12c), the present scheme became as dissipative as the HLLE scheme locally at the leading edge due to the strong expansion. As a result, the vortices were smeared out as shown in Fig. 2b. By implementing Eq. (12), the resolution of the resulting scheme remains as good as the Roe scheme, while the scheme is robust enough to prevent the carbuncle problem.

Acknowledgment

References

[1]Einfeldt, B., "On Godunov-Type Methods for Gas Dynamics," *SIAM Journal of Numerical Analysis,* Vol. 25, No. 2, April 1988, pp. 294–318.

[2]Einfeldt, B., Munz, C. D., Roe, P. L., and Sjögreen, B., "On Gudonov-Type Methods Near Low Densities," *Journal of Computational Physics,* Vol. 92, No. 2, 1991, pp. 273–295.

[3]Wada, Y., "An Improvement of the HLLEM Scheme and Its Extension to Chemically Reacting Flows," Second U.S. National Congress on Computational Mechanics, Washington, DC, Aug. 1993.

[4]Roe, P. L., "Approximate Riemann Solvers, Parameter Vectors, and Difference Scheme," *Journal of Computational Physics,* Vol. 43, No. 2, 1981, pp. 357–372.

[5]Quirk, J. J., "A Contribution to the Great Riemann Solver Debate," Institute for Computer Applications in Science and Engineering, ICASE Rept. 92-64, Nov. 1992.

[6]Obayashi, S., and Goorjian, P. M., "Improvements and Applications of a Streamwise Upwind Algorithm," AIAA Paper 89-1957, June 1989.

Numerical Investigation of Cylinder Wake Flow with a Rear Stagnation Jet

J. D. Mo and M. R. Duke Jr.*
Memphis State University, Memphis, Tennessee 38152

I. Introduction

WAKE flow characteristics behind a cylinder have been a topic of interest for years. Various means have been applied to attempt to eliminate the wake since the momentum deficit in the wake creates a considerable drag and an oscillating lateral force that causes mechanical vibrations on the cylinder. Upon visualization of the flow past a cylinder with a rear stagnation jet,[1,2] the flow appears fully attached as conventional inviscid flow does. Therefore, at first glance, it would be suspected that the form drag on the cylinder has been reduced to zero as predicted by inviscid flow theory. However, a detailed numerical simulation reveals that the form drag coefficient increases as the jet velocity increases. The mechanics of the increasing form drag will be addressed in this Note.

II. Computational Approach

A. Physical and Mathematical Model

The physical model for the numerical study is shown in Fig. 1. In this model, a stationary cylinder of radius R is placed in a uniform flow U_∞. A jet is located at the rear stagnation point with an area-averaged velocity V_j and jet direction parallel with the oncoming flow. For geometric simplicity, a polar coordinate (r, θ) system is adopted and is defined in Fig. 1.

The incompressible flow was treated as laminar because we were interested in Reynolds numbers, based on cylinder diameter, that were less than 2500. The Navier-Stokes equations in primitive variables are given as

$$\frac{\partial u_r}{\partial r} + \frac{u_r}{r} + \frac{\partial u_\theta}{r\,\partial\theta} = 0 \tag{1}$$

$$\frac{\partial u_r}{\partial t} + u_r\frac{\partial u_r}{\partial r} + u_\theta\frac{\partial u_r}{r\,\partial\theta} - \frac{u_\theta^2}{r} = -\frac{1}{\rho}\frac{\partial P}{\partial r}$$

$$+ \nu\left(\frac{\partial^2 u_r}{\partial r^2} + \frac{1}{r}\frac{\partial u_r}{\partial r} + \frac{1}{r^2}\frac{\partial^2 u_r}{\partial\theta^2} - \frac{2}{r^2}\frac{\partial u_\theta}{\partial\theta} - \frac{u_r}{r^2}\right) \tag{2a}$$

$$\frac{\partial u_\theta}{\partial t} + u_r\frac{\partial u_\theta}{\partial r} + u_\theta\frac{\partial u_\theta}{r\,\partial\theta} + \frac{u_r u_\theta}{r} = -\frac{1}{\rho}\frac{\partial P}{r\,\partial\theta}$$

$$+ \nu\left(\frac{\partial^2 u_\theta}{\partial r^2} + \frac{1}{r}\frac{\partial^2 u_\theta}{\partial r} + \frac{1}{r^2}\frac{\partial^2 u_\theta}{\partial\theta^2} + \frac{2}{r^2}\frac{\partial u_r}{\partial\theta} - \frac{u_\theta}{r^2}\right) \tag{2b}$$

Traditionally, Eqs. (2) are solved for velocity, and Eq. (1) is solved for pressure. However, pressure does not appear in the continuity equation, but a Poisson equation for pressure can be directly derived from the continuity and momentum equations,

$$\nabla^2 P = -\frac{2}{r}\left[\frac{\partial u_\theta}{\partial r}\left(\frac{\partial u_r}{r\partial\theta}-u_\theta\right)-\frac{\partial u_r}{\partial r}\left(\frac{\partial u_\theta}{r\partial\theta}+u_r\right)\right] \qquad (3)$$

The governing differential equations (2) for velocity are parabolic, and the equation for pressure, Eq. (3), is elliptic. To solve these differential equations, proper boundary and initial conditions must be specified. A no-slip condition was applied for the velocity solution at the cylinder surface. A nonreflective extrapolation was employed to establish the external boundary condition. The external boundary was located 43 diameters away from the cylinder surface. The boundary condition for pressure at the cylinder surface is

$$\frac{\partial p}{\partial n} = \frac{1}{Re}\frac{\partial\zeta}{\partial s} \qquad (4)$$

where n is the local surface normal, ζ is the vorticity, and s is the local surface direction. This boundary condition is directly derived from the no-slip wall boundary condition. When the rear stagnation jet is in operation, the jet velocity at the exit is specified, and the pressure at the jet exit equals the ambient local static pressure. This ambient pressure was obtained by averaging the pressures on each side of the jet on the cylinder surface.

An inviscid flow past a cylinder was used to provide an initial condition for the flow analysis without the jet. The viscous effects
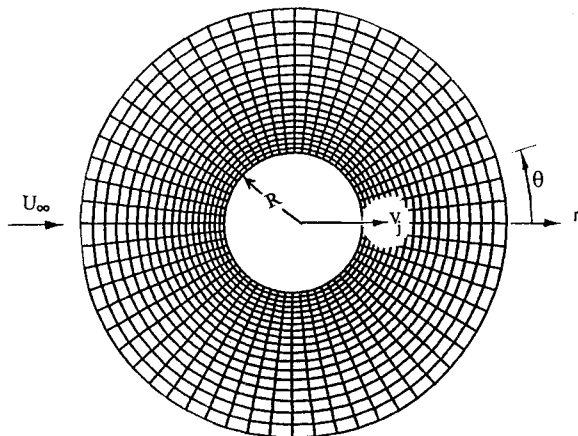

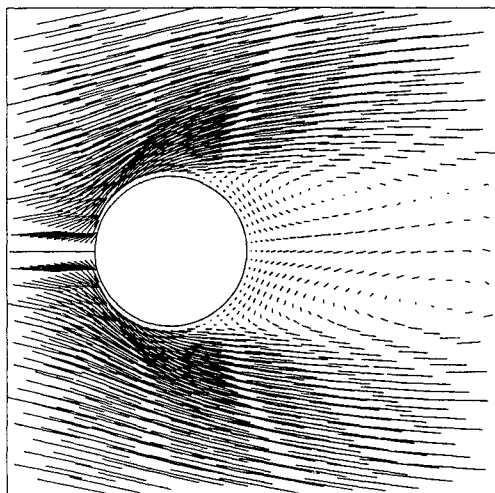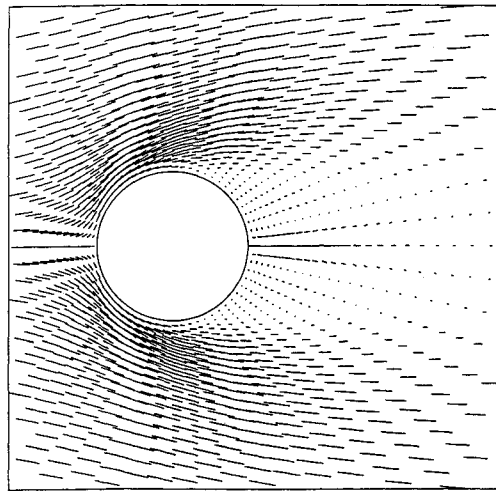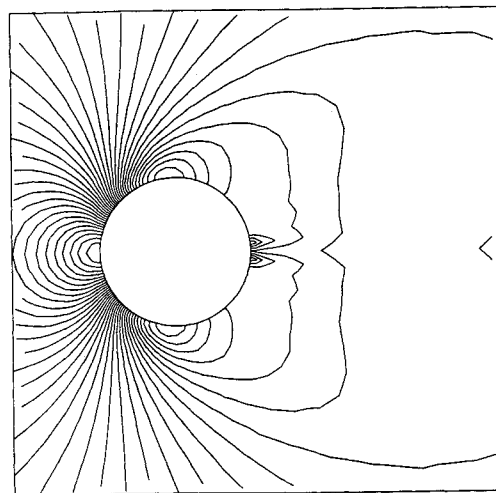Fig. 1 Physical model and computational grid.

Fig. 2 Computed fully developed conventional wake flowfields with $Re = 700$ and time = 50.0.

a) velocity vector plot,

b) pressure contour plot

Fig. 3 Computed wake flowfields at jet velocity ratio 1.0 with $Re = 700$.

of the fluid were then applied, and the computations were continued until the von Kármán vortex street was fully achieved. This fully developed flow solution was used as the initial starting flowfield when the subsequent numerical simulations were computed for the flow with the jet.

B. Numerical Procedures

To improve the numerical accuracy, a nonuniform grid was chosen that allocated more grid points near the cylinder surface, as shown in Fig. 1.
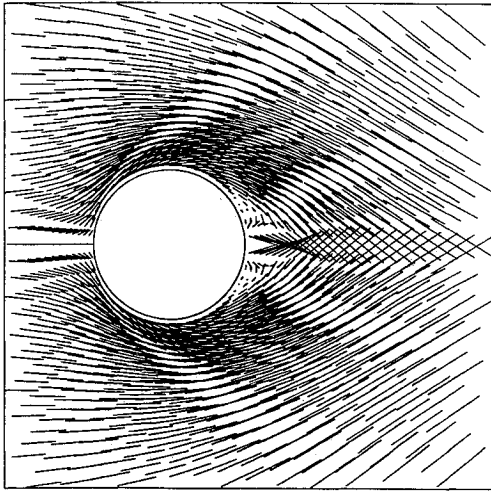
In this work, the numerical solution is pursued through the direct solution of the Poisson pressure equation with pressure correction to ensure mass conservation. The momentum equations are solved by handling the viscous terms implicitly and the advection terms semi-implicitly as

$$\frac{V^{n+1}-V^n}{\Delta t} + (V^n\cdot\nabla)V^{n+1} = -\nabla P^n + Re^{-1}\nabla^2 V^{n+1} \qquad (5)$$
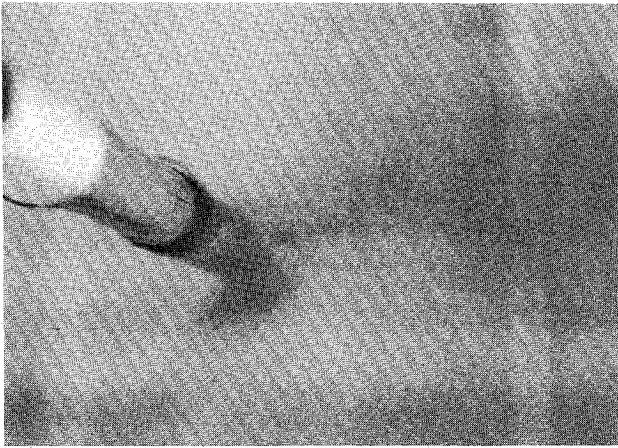
where Δt is the time-step interval. The convective terms are upwind finite differenced, and the diffusive terms are central differenced. Once the velocity is solved from Eq. (5), the pressure can be determined by

$$\nabla^2 P^{n+1} = -(V^n\cdot\nabla)V^{n+1}+\frac{\nabla\cdot V^n}{\Delta t} \qquad (6)$$

The last term in Eq. (6) is for the pressure correction to force mass conservation. By using a central difference approximation

a) Velocity vector plot

b) Pressure contour plot

Fig. 4 Computed and visualized wake flowfields at jet velocity ratio 23.

A. Conventional Wake Flow Simulation

For the flow past a cylinder, the primary region of interest is the area in the vicinity of the cylinder wall and the area downstream of the cylinder. Therefore, all figures will be magnified views of the physical plane in these regions. A flowfield with a well-developed conventional von Kármán vortex street is shown in Fig. 2. This flowfield only serves as the starting point for the subsequent flow simulation when the jet is in operation.

B. Wake Flow Response to the Rear Stagnation Jet

The alternating nature of the wake lies in the oscillation of the rear stagnation point. When a rear stagnation jet is in operation, the oscillation of the rear stagnation point is stopped. The minimum value of V_j needed to generate a symmetric wake flow was not determined, but Fig. 3a shows a steady velocity field for the flow over a cylinder fitted with a rear stagnation jet operating at V_j/U_∞ = 1.0. It can be seen that the flow separation point has moved downstream when compared with Fig. 2, in which there is no rear stagnation jet. Figure 3b shows the corresponding pressure contours. When the pressure distribution is examined, the flowfield appears symmetric. Extensive numerical experiments revealed that the flow separation point moves further toward the rear stagnation point and the recirculating bubbles become smaller as the jet velocity increases. To compare the numerical solutions with the flow visualization results, Fig. 4a shows a computed steady flowfield with a jet operating at V_j/U_∞ = 23.0, and Fig. 4b shows the visualized wake flow pattern at the same conditions. The computed and the experimental results appear to be in fairly good agreement with each other. The alternating wake has been eliminated, and the flow appears as if inviscid.

At first glance, it would be suspected that the form drag on the cylinder has been reduced to zero as predicted by inviscid flow theory. However, Fig. 5 shows the form drag acting on the cylinder by numerically integrating the surface pressure. It can be seen that the form drag increases with increasing jet velocity. The reason for the increasing drag is the decrease in the surface pressure of the cylinder as the jet velocity increases, as shown in Fig. 6. Examination of the pressure solution shows no lateral force.

and a successive-over-relaxation (SOR) algorithm, the pressure solution is obtained by iteration as follows:

$$(P_{i,j}^{n+1})^{k+1} = (P_{i,j}^{n+1})^k - \lambda\Delta\zeta^2\left[(V^n\cdot\nabla)V^{n+1} + \frac{\nabla\cdot V'^n}{\Delta t}\right]$$

$$- \lambda\left[(P_{i+1,j}^{n+1} + P_{i-1,j}^{n+1})^k + h^2(P_{i,j+1}^{n+1} + P_{i,j-1}^{n+1})^k + (P_{i,j}^{n+1})\right] \quad (7)$$

in which the superscript k is the iteration index, λ is the relaxation factor, and h is the grid aspect ratio, defined as $\Delta\zeta/\Delta\eta$.

III. Numerical Results and Discussions

The numerical computations of this research work consisted of two parts. In the first part, an unsteady flow around the cylinder was simulated. This flow was impulsively started and developed into an alternating oscillating wake flow as discussed in the previous section. After a fully developed von Kármán vortex street was established, the rear stagnation jet was started. The computations were conducted on an IRIS-4D workstation located in the Computational Fluid Dynamics Laboratory at Memphis State University.

The relaxation factor λ was 1.85, and this value was used for all of the calculations presented in this work. The grid size was fixed at 61 × 61. Since the numerical scheme used had an implicit nature, no numerical instability due to the time-step size was encountered. By only considering the accuracy requirement, the dimensionless time step was taken as 0.05.
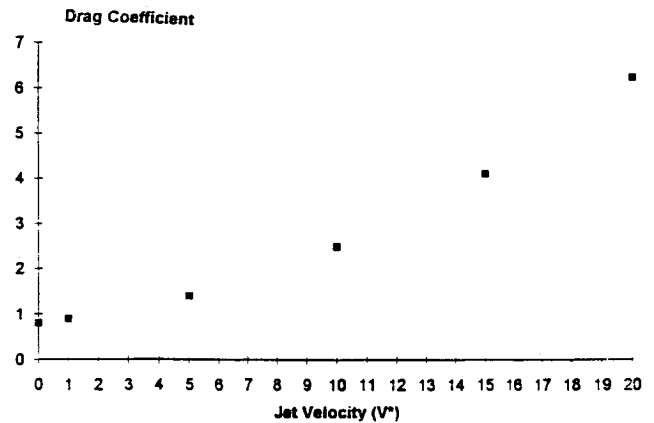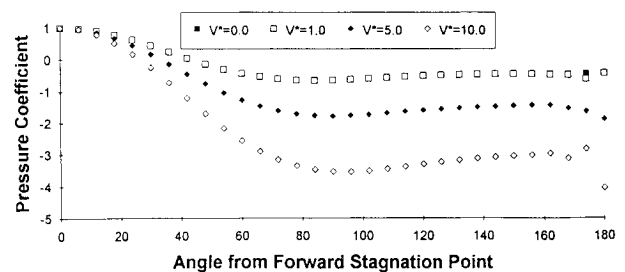

Fig. 5 Form drag on cylinder vs jet velocity (Re = 200).

Fig. 6 Surface pressure distribution vs jet velocity (Re = 200).

IV. Conclusions

The following conclusions were drawn from this study.

1) Flow behind a cylinder can be effectively influenced by a rear stagnation jet. The computational results are in good agreement with the experimental flow visualization.

2) The unsymmetric wake flow becomes symmetric when the rear stagnation jet is in operation with a velocity ratio as low as 1. The size of the symmetric recirculation region becomes smaller as the jet speed increases.

3) A rear stagnation jet forces a symmetrical wake flow pattern, thus eliminating the lateral force.

4) The pressure on the cylinder surface decreases over the entire surface, but significantly more on the downstream side of the cylinder, as the jet velocity increases, causing an increase in form drag as jet velocity ratio increases.

5) The rear stagnation jet to significantly increase form drag on a bluff body has direct applications in aerodynamic controls of re-entry or flights at high angles of attack.

References

[1]Duke, M. R., Jr., "Effects of a Rear Stagnation Jet on the Wake Flow Behind a Cylinder," M.S. Thesis, Dept. of Mechanical Engineering, Memphis State Univ., Memphis, TN, Dec. 1992.

[2]Duke, R., Shrader, B., and Mo, J., "Effects of a Rear Stagnation Jet on the Wake Behind a Cylinder," *AIAA Journal*, Vol. 31, No. 9, 1993, pp. 1727–1729.

Surface Interference in Rayleigh Scattering Measurements near Forebodies

Zaidi B. Zakaria* and Steven H. Collicott†
Purdue University, West Lafayette, Indiana 47907

I. Introduction

HIGH-SPEED boundary-layer transition on forebodies is currently a topic of considerable interest.[1] Transition experiments in quiet-flow supersonic facilities[2] require nonintrusive diagnostics. Some form of Rayleigh scattering measurement is desirable in these flows because calibrated hot-wire measurements are elusive.[3] Rayleigh scattering measurements of density are feasible in various fluid flow experiments.[4-6] The simplest and least expensive method is to detect the scattered light without any spectral filtering. This permits use of an Nd:YAG laser without injection seeding. Thus if direct (unfiltered) Rayleigh scattering may be used rather than filtering the Doppler-shifted scattered light from an extremely stable narrow-band laser, considerable costs savings may be had.

Direct Rayleigh scattering is known to not be feasible near surfaces. Numerous flows of interest, such as boundary layers and the region between a blunt body and a bow shock, are near the surface. Thus experiments to quantify this near-body limit on forebodies are performed. The distance from the forebody within which one is forced to use a filtered Rayleigh technique must be known for proper experiment design. The question of how close to the forebody is too close is addressed by this experiment.

II. Theoretical Background

The energy per unit of solid angle of the light scattered by gas molecules in the direction perpendicular to the incident beam and its polarization vector is[7]

$$E_s = E_0 \sigma_s (3NV/8\pi) \qquad (1)$$

*Student Research Assistant, School of Aeronautics and Astronautics.
†Assistant Professor, School of Aeronautics and Astronautics.

where E_0 is the incident areal energy density, σ_s is the scattering cross section of the gas molecules, N is the number density of the gas, and V is the measurement volume in the gas. The total scattered energy, for optics collecting scattered light within a solid angle of $\Omega \ll 4\pi$, is then approximately

$$E_t = E_0 \sigma_s (3NV/8\pi)\Omega \qquad (2)$$

Furthermore, since the number density of the gas is $N = \rho/m$, where ρ is the density of the gas and m is the mass of the gas per molecule, Eq. (2) can be written as

$$E_t = (3/8\pi)(\rho/m)V\Omega\sigma_s E_0 \qquad (3)$$

To calculate the scattering volume, the incident beam is assumed to have a Gaussian distribution. Furthermore, since the radius of the pinhole on the photomultiplier tube (PMT) is larger than the image of the beam waist, a cylindrical volume is assumed. The cylinder has a circular area with the radius of the beam waist and a length equal to the diameter of the area captured by the PMT. Thus, the scattering volume V for the experiment is

$$V = [d_p/M_c][\lambda f/w]^2 \qquad (4)$$

where d_p is the diameter of the pinhole of the PMT, M_c is the magnification of the collection optics, λ is the wavelength of the laser, f is the focal length of the focusing lens, and w is the radius of the incident beam incident on the focusing lens.

III. Experiment Description

The geometry and components of the experiment are shown schematically in Fig. 1. A Q-switched frequency doubled Nd:YAG laser produced the beam that is focused by a lens (focal length = 100 mm). A low-speed (≈ 1 m/s) jet of nitrogen is allowed to flow through the focal volume. The nitrogen is used to minimize the presence of dust particles that would scatter more efficiently and obscure the Rayleigh scattered light. A sample of the beam is detected by an energy meter to determine the energy of the incident beam, whereas the scattered energy is imaged perpendicularly onto the PMT. Because of the need for uninterrupted propagation on both sides of the beam waist, the geometry described is probably not a good candidate for use over winglike surfaces. A tight stack of razor blades is stacked behind the jet to provide a nonreflecting background. The oscilloscope is trigged by the Nd:YAG so that there is reliable detection.

Following calibration of the PMT, light scattered from room temperature and pressure nitrogen is measured to insure that Rayleigh scattering is detected by the experiment. Approximately 10^{-15} J from a 0.1-J laser pulse is collected. This corresponds to an average power incident on the PMT of approximately 0.1μW during the duration of the 10-ns pulse. The observed signal is within 15% of the expected value calculated with the assumed cylindrical scattering volume. The error is primarily due to the assumption that the beam exhibited a Gaussian distribution, whereas physically the transverse mode structure of the Nd:YAG beam is complex. Because the scattering volume V is identical for every measurement in this experiment, and the results are normalized, the error in V does not affect the results. That is, the results are a measure of scattering per volume, independent of how accurately that volume is computed. Of course, if the data presented later had been acquired from different scattering spots, this would not be true. Application of these measurements to other beam waist sizes can be made by scaling with the Gaussian beam radius. Recall that the purpose of this experiment is to provide general data for experiment design and evaluation of the relative merits of various techniques, not to determine the minimum separation for a specific laser spot or aerodynamic model.

Nine different cylinders are used as representative test models. The surfaces of the nine bodies are in three categories: unpolished, polished, and painted flat black over a polished surface. In each category, there is a "thin" body (diameter = 4 mm), a "medium" body (diameter = 8 mm), and a "thick" body (diameter = 13 mm).